*Journal of Sound and Vibration* (1999) **222**(1), 19–47
*Article No*. jsvi.1998.1986, available online at http://www.idealibrary.com on IDEAL

# DYNAMIC STABILITY OF A ROTATING SHAFT DRIVEN THROUGH A UNIVERSAL JOINT

A. J. MAZZEI JR

*Department of Mechanical Engineering and Applied Mechanics,*
*The University of Michigan, G044 W.E. Lay Automotive Laboratory,*
*1231 Beal Avenue, Ann Arbor, MI, 48109-2121, U.S.A.*

A. ARGENTO

*Department of Mechanical Engineering, The University of Michigan—Dearborn,*
*4901 Evergreen Rd, Dearborn, MI, 48128-1491, U.S.A.*

AND

R. A. SCOTT

*Department of Mechanical Engineering and Applied Mechanics,*
*The University of Michigan, G044 W.E. Lay Automotive Laboratory,*
*1231 Beal Avenue, Ann Arbor, MI, 48109-2121, U.S.A.*

(*Received* 11 *May* 1998, *and in final form* 21 *September* 1998)

The dynamic stability of a system composed of driving and driven shafts connected by a universal joint is investigated. Due to the characteristics of the joint, even if the driving shaft experiences constant torque and rotational speed, the driven shaft experiences fluctuating rotational speed, bending moments and torque. These are sources of potential parametric, forced and flutter type instabilities. The focus of this work is on the lateral instabilities of the driven shaft. Two distinct models are developed, namely, a rigid body model (linear and non-linear) and a flexible model (linear). The driven shaft is taken to be pinned at the joint end and to be resting on a compliant damped bearing at the other end. Both models lead to sets of differential equations with time dependent coefficients. For both rigid (linear and non-linear) and flexible models, flutter instabilities were found but occurred outside the practical range of operation (rotational speed and torque) for lightly damped systems. Parametric instability charts were obtained by using the monodromy matrix technique for both rigid and flexible linear models. The transmitted bending moments were found to cause strong parametric instabilities in the system. By comparing the results from the two linear models, it is shown that the inclusion of flexibility leads to new zones of instability, not predicted by previous models. These zones, depending on the physical parameters of the system, can occur for practical conditions of operation. Using direct numerical integration for a few sets of specific parameter values, forced resonances were found when the rotational speed reached a value equal to a natural frequency of the system divided by two.

0022–460X/99/160019 + 29 $30.00/0

## 1. INTRODUCTION

Universal joints, commonly referred to as U-Joints, are widely used in rotary machines when transmission of torque or power is needed between two shafts that are not collinear. Although a non-constant velocity joint, the U-Joint is extensively used in preference to other types of joints. The principal advantages of it are its relatively low manufacturing cost, simple and rugged construction, long life, and ease of serviceability. Also, in addition to providing the necessary torque capacity in a limited operating space, the U-Joint has the capability to withstand relatively high externally imposed axial forces and relatively high operational speeds.

In systems driven by U-Joints, instabilities of several types can occur, for example, flutter, parametric, and forced. To fully analyze these instabilities mechanical models involving U-Joints and rotating shafts need to be developed incorporating the physics which produce the instabilities.

The present work deals with the dynamic stability of rigid and flexible shafts mounted in a compliant damped support and driven through a U-Joint. The focus is on the lateral instabilities of the shaft, and the effects of bearing compliance and damping and system geometric parameters.

A brief review of the salient literature will now be given.

The literature on rotating shafts is very extensive, because of the numerous technical applications. Citations to early work can be found in H. P. Lee *et al*. [1], in their paper on a rotating Timoshenko shaft. The recent work of C. W. Lee and Yun [2] should also be noted. Guidelines to some of the modelling employed here were obtained from the work of Eshleman and Eubanks [3] on the critical speeds of rotating shafts.

The literature on stability, and the use of follower and non-follower forces and moments, is equally extensive. The classic works of Ziegler [4] and Leipholz [5] contain numerous instructive examples. The field continues to be fruitful, as the works of Khader [6] on follower loads, Plaut and Wauer [7] on parametric, external and combination resonances, and the text by C. W. Lee [8] attest.

Work on drive systems containing U-Joints is not so extensive. Lateral and torsional vibrations of a rotating shaft driven by a universal joint were investigated by Ota *et al*. [9, 10]. There the moment applied by the U-Joint to the driven shaft was modelled as a non-follower one. The driven shaft was taken to be a massless flexible shaft with an off-center symmetric rotor. The flexibility of the shaft was included in the formulation as a lumped stiffness, rather than distributed. Parametric resonances were found to be possible when the angular velocity of the driving shaft was close to an even integer (or sub-multiple) of a torsional or lateral natural frequency of the driven shaft. In a later work [11] Kato and Ota investigated the lateral vibrations of a rotating shaft driven by a U-Joint with friction, the moment due to the friction being modelled as a non-follower one.

The effects of joint angles and joint friction in a double universal joint system were investigated by Sheu *et al*. [12]. Using Rayleigh beam theory they found that the values of the critical speeds for the intermediate shaft are affected by the axial torques, which depend on viscous friction coefficients and joint angles.

Saigo *et al*. [13] considered the dynamics of a multi shaft, multi U-Joint system. They showed that Coulomb friction in one of the U-Joints could lead to unstable motions. However, the shafts were treated as rigid and the fluctuations of rotational speeds due to the U-Joint were taken to be negligible. Also, their modelling is such that time dependent coefficients do not appear in the equations of motion so parametric instabilities can not be addressed.

Torsional instabilities, due to fluctuating angular velocity, in a driveline imcorporating a U-Joint were investigated by Asokanthan and Hwang [14] and Asokanthan and Wang [15]. The system was modelled as a two-degree-of-freedom system with damping. Analytical conditions for the onset of parametric instability were derived and the occurrence of combination resonance of the sum type was identified while the combination resonance of the difference type was shown to be absent. Damping was found to stabilize the system in the sub-harmonic case and to destabilize the system in the combination case. For a given joint angle the critical speed ranges to be avoided for stable operation were obtained. Based on these works it is seen that both torsional and lateral instabilities can occur in U-Joint systems. In the present work the focus is on shafts whose properties are such that the bending natural frequencies are much less than the torsional natural frequencies. Hence, torsional motions are neglected.

The influence of joint angle on the critical speed behavior of a shaft driven through a U-Joint was investigated by Rosenberg [16]. In that work the shaft was modelled as a massless uniform elastic shaft with a concentrated mass at its midpoint. The transmitted torque was taken to be a follower one. There the only bending moments considered were those due to bending components of the follower torque, whereas a U-Joint also produces direct bending components. It was found that when the joint angle was different from zero, parametric instabilities could arise.

Transverse vibrations and stability of a rigid driven shaft in a U-Joint system with springs and dampers and zero initial joint angles were analyzed by Iwatsubo and Saigo [17]. It was found that parametric and flutter type instabilities could arise. The relative role of system damping and stiffness was investigated.

Several possibly important issues have not so far been addressed in the literature, to the authors' knowledge. Most importantly, the effects of distributed shaft flexibility and inertia on parametric resonances have not been explored. Also, effects of non-zero initial joint angles and system non-linearities need to be assessed. These issues are explored in this paper, with the major emphasis being on the role of distributed shaft flexibility and inertia.

The plan for the paper is as follows. Section 2 introduces a model, similar to Iwatsubo and Saigo's model, in which the driven shaft is regarded as rigid. However, the initial joint angles are taken to be non-zero and some non-linear effects are taken into account. In Section 3 a flexible model (linear) for the driven shaft is developed. Galerkin's method is applied to the equations of motion for the flexible model in Section 4. In sections 5 and 6 flutter type instabilities and parametric type instabilities are examined for both models. Section 7 gives some preliminary results for the rigid non-linear model, obtained using direct numerical integration, and in section 8 forced resonances are investigated.

## 2. EQUATIONS OF MOTION: RIGID BODY MODEL

Figure 1 shows a shaft $AB$ of length $l$ driven through a U-Joint by a driving shaft $BC$ which spins at constant angular velocity $\Omega$. Springs and dampers are connected to the driven shaft at $A$ as shown.

Two inertial frames are used in the derivation of the equations of motion due to the presence of the driving and driven shafts. $XYZ$ is a fixed frame with origin at the center of the cross with $Z$ directed along the driving shaft. $X$ and $Y$ are arbitrarily oriented in the crosspiece section. $xyz$ is a fixed frame defining the undeflected orientation of the driven shaft, with origin at the center of the crosspiece and $z$ directed along the axis (see Figure 2). $xyz$ can be obtained from $XYZ$ by a sequence of rotations. A rotation $\alpha_0$ about $Y$ leads to the intermediate axes $x_iy_iz_i$. A second rotation $\delta_0$ about $x_i$ leads to the configuration $xyz$ ($\alpha_0$ and $\delta_0$ are called initial joint angles).

A moving frame is attached to the shaft on its central axis and is described by Euler angles $\beta$ and $\gamma$. First a rotation $\beta$ about $y$ leads to the intermediate axes $x_1y_1z_1$ as shown in Figure 2. Then a rotation $\gamma$ about $x_1$ leads to the final configuration of the moving axes $x_2y_2z_2$. The moving frame does not spin with the shaft.

Let $\boldsymbol{\omega}_2$ be the angular velocity of the moving frame $x_2y_2z_2$ with respect to the inertial frame $xyz$. The angular velocity of the driven shaft with respect to the moving frame $x_2y_2z_2$ is called $\boldsymbol{\omega}$. The modified version of Euler's equations [18]

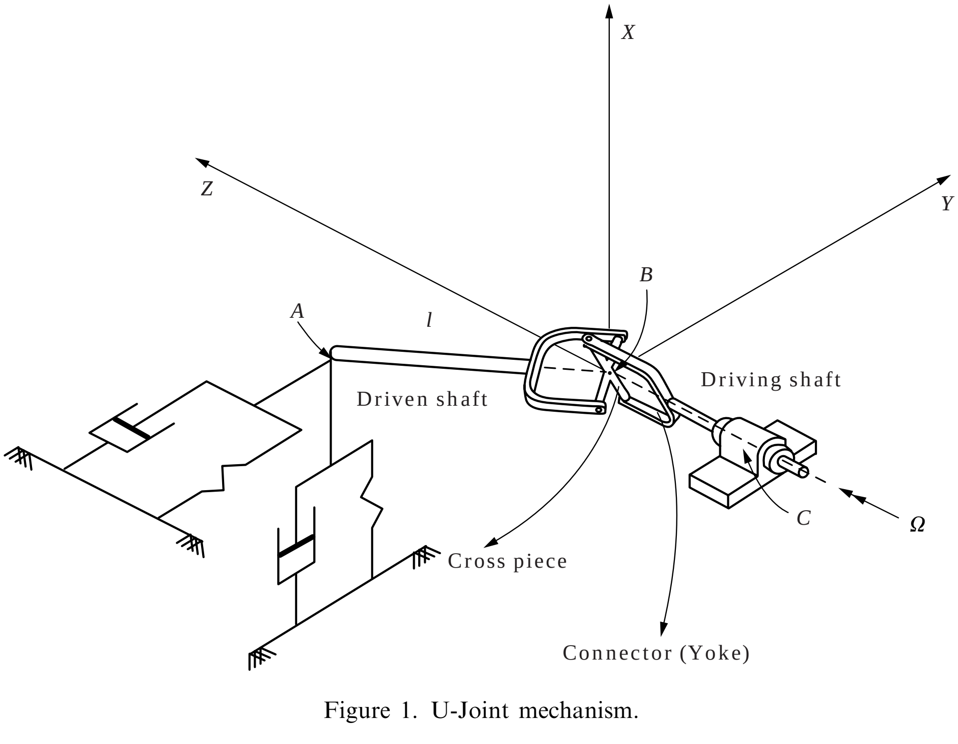

Figure 1. U-Joint mechanism.

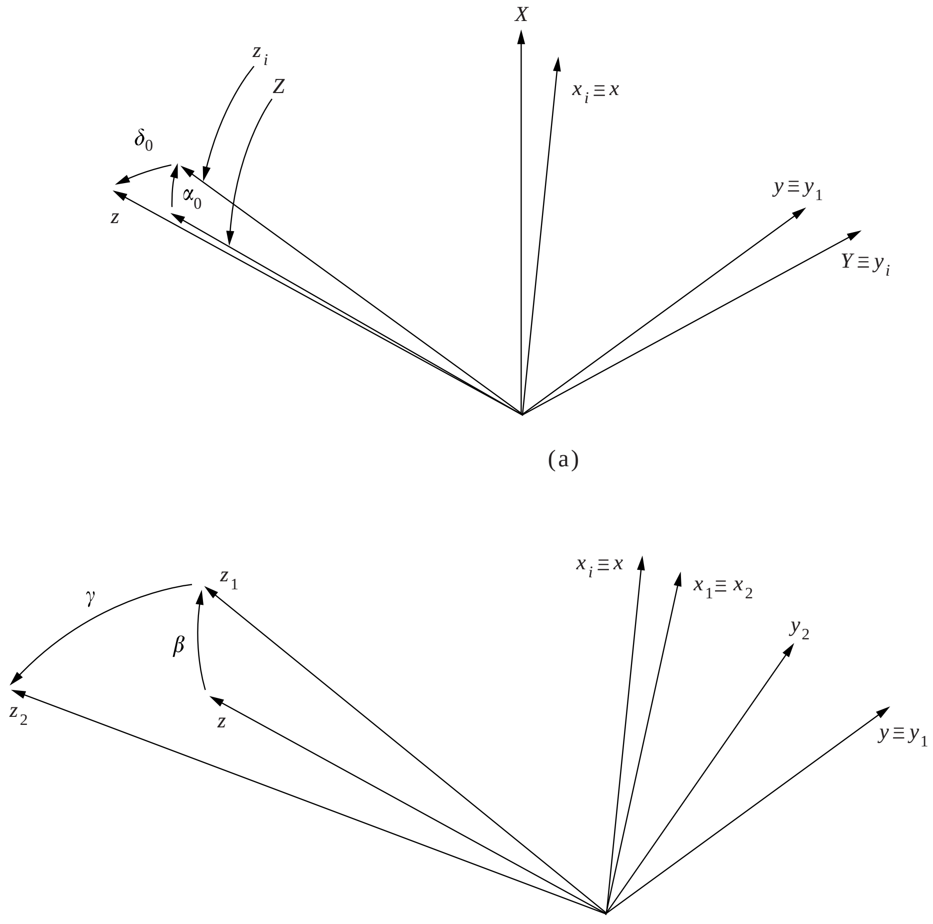

(a)

(b)

Figure 2. Reference frames: (a) rotations $\alpha_0$ and $\delta_0$, (b) rotations $\beta$ and $\gamma$.

is used (here, the symmetry axis about which the moving frame $x_2y_2z_2$ rotates is the driving shaft axis), namely

$$\sum M_{x_2,o} = J_{x_2,o}\dot{\omega}_{x_2} - (J_{y_2,o} - J_{z_2,o})\omega_{y_2}\omega_{z_2} + J_{z_2,o}\omega\omega_{y_2}, \tag{1}$$

$$\sum M_{y_2,o} = J_{y_2,o}\dot{\omega}_{y_2} - (J_{z_2,o} - J_{x_2,o})\omega_{z_2}\omega_{x_2} - J_{z_2,o}\omega\omega_{x_2}, \tag{2}$$

$$\sum M_{z_2,o} = J_{z_2,o}(\dot{\omega}_{z_2} + \dot{\omega}). \tag{3}$$

Here, $M_{a,b}$ is the moment about axis $a$ with respect to reference point $b$, $J$'s are mass moments of inertia with respect to point $O$, and overdots denote differentiation with respect to time. The third equation would give the load torque if desired and will not appear in the sequel.

Here,

$$\boldsymbol{\omega}_2 = \dot{\beta}\cos(\gamma)\hat{\mathbf{j}}_2 - \dot{\beta}\sin(\gamma)\hat{\mathbf{k}}_2 + \dot{\gamma}\hat{\mathbf{i}}_2 \tag{4}$$

and

$$\dot{\boldsymbol{\omega}}_2 = \ddot{\gamma}\hat{\mathbf{i}}_2 + (\ddot{\beta}\cos(\gamma) - \dot{\beta}\dot{\gamma}\sin(\gamma))\hat{\mathbf{j}}_2 - (\ddot{\beta}\sin(\gamma) + \dot{\beta}\dot{\gamma}\cos(\gamma))\hat{\mathbf{k}}_2, \tag{5}$$

where $\hat{\mathbf{i}}_2$, $\hat{\mathbf{j}}_2$ and $\hat{\mathbf{k}}_2$ denote unit vectors in the $x_2$, $y_2$, and $z_2$ directions, respectively.

Assuming that the initial joint angles are small, such as usually occurs in practice, the rotational speed of the driven shaft can be written as (see, for example, reference [19]):

$$\omega \equiv \Omega p_2(t) = \Omega\left[1 - \frac{\alpha_0^2}{2}(1 - \cos(2\Omega t)) - \frac{\delta_0^2}{2}(1 + \cos(2\Omega t)) - \alpha_0\delta_0\sin(2\Omega t)\right], \tag{6}$$

where $\Omega$ is the rotational speed of the driving shaft.

Substitution of equations (4), (5) and (6) into equations (1) and (2) leads to

$$\sum M_{x_{2,o}} = J_{x_{2,o}}\ddot{\gamma} + (J_{y_{2,o}} - J_{z_{2,o}})\dot{\beta}^2\cos(\gamma)\sin(\gamma) + J_{z_{2,o}}\dot{\beta}\cos(\gamma)\Omega p_2(t), \tag{7}$$

$$\sum M_{y_{2,o}} = J_{y_{2,o}}(\ddot{\beta}\cos(\gamma) - \dot{\beta}\dot{\gamma}\sin(\gamma)) + (J_{z_{2,o}} - J_{x_{2,o}})\dot{\beta}\dot{\gamma}\sin(\gamma) - J_{z_{2,o}}\dot{\gamma}\Omega p_2(t). \tag{8}$$

The next step is to calculate the moments resolved on the moving system. Here the driven shaft is taken to be pinned at the end coinciding with the U-Joint center and to rest on a compliant bearing at the other end. The bearing is modelled by pairs of springs and dampers (see Figure 1).

In the model used here the spring and damper forces are given by

$$\mathbf{F}_s = -K_x l\sin(\beta)\hat{\mathbf{i}}_2 + K_y l\sin(\gamma)\cos(\beta)\hat{\mathbf{j}}_2, \tag{9}$$

$$\mathbf{F}_d = -C_x l\dot{\beta}\cos(\gamma)\hat{\mathbf{i}}_2 + C_y l\dot{\gamma}\hat{\mathbf{j}}_2, \tag{10}$$

where $K$ stands for spring stiffness and $C$ stands for the viscous damping coefficient.

For two perpendicular springs ($K_x$, $K_y$) and two perpendicular dampers ($C_x$, $C_y$) directed along $x$ and $y$, respectively, the moments that arise at the center of the U-Joint can be expressed as

$$\mathbf{M}_o^s = -(l^2K_y\sin(\gamma)\cos(\beta))\hat{\mathbf{i}}_2 - (l^2K_x\sin(\beta))\hat{\mathbf{j}}_2, \tag{11}$$

$$\mathbf{M}_o^d = -(l^2C_y\dot{\gamma})\hat{\mathbf{i}}_2 - (l^2C_x\dot{\beta}\cos(\gamma))\hat{\mathbf{j}}_2. \tag{12}$$

The next step is to obtain the components of the moment transmitted by the U-Joint. The transmitted moment acts along the normal unit vector to the crosspiece (see, for example, reference [19]) which is given by

$$\mathbf{e}_n = e_{nx_2}\hat{\mathbf{i}}_2 + e_{ny_2}\hat{\mathbf{j}}_2 + e_{nz_2}\hat{\mathbf{k}}_2, \tag{13}$$

where

$$e_{nx_2} = -\frac{1}{\varepsilon}\,[\cos(\tau)\beta - \cos(\tau)\alpha_0\gamma\delta_0 + \cos(\tau)\alpha_0 - \sin(\tau)\gamma - \sin(\tau)\delta_0] \times [\cos(\tau) - \cos(\tau)\beta\alpha_0 + \sin(\tau)\beta\alpha_0], \tag{14}$$

$$e_{ny_2} = -\frac{1}{\varepsilon}\,[\cos(\tau)\beta - \cos(\tau)\alpha_0\gamma\delta_0 + \cos(\tau)\alpha_0 - \sin(\tau)\gamma - \sin(\tau)\delta_0] \times [\cos(\tau)\gamma\beta + \cos(\tau)\alpha_0\delta_0 + \cos(\tau)\alpha_0\gamma + \sin(\tau) - \sin(\tau)\gamma\delta_0], \tag{15}$$

$$e_{nz_2} \equiv \varepsilon = \sqrt{\begin{array}{l}[\cos(\tau)\gamma\beta + \cos(\tau)\alpha_0\delta_0 + \cos(\tau)\alpha_0\gamma + \sin(\tau) - \sin(\tau)\gamma\delta_0]^2 \\ \quad + [\cos(\tau) - \cos(\tau)\beta\alpha_0 + \sin(\tau)\beta\delta_0]^2\end{array}} \tag{16}$$

and $\tau = \Omega t$.

The moment that the U-Joint applies to the driven shaft is

$$\mathbf{M} = M\mathbf{e}_n, \tag{17}$$

where $M$ can be shown to be related to the torque that acts on the driving shaft, $T_0$, by

$$M = \frac{T_0}{\hat{\mathbf{e}}_n \cdot \hat{\mathbf{K}}}, \tag{18}$$

in which $\hat{\mathbf{K}}$ denotes the unit vector in the $Z$ direction.

Substitution of equations (4), (5), (11), (12), (17) and (18) in equations (1) and (2) leads to the following set of non-linear ordinary differential equations:

$$v^2\ddot{\gamma} + (1-\eta)\dot{\beta}^2 v^2 \cos(\gamma)\sin(\gamma) + \eta\dot{\beta}v^2\cos(\gamma)p_2(\tau) = \tilde{M}_{x_2} - \tilde{K}_y \sin(\gamma)\cos(\beta) - \tilde{C}_y v\dot{\gamma}, \tag{19}$$

$$v^2\ddot{\beta}\cos(\gamma) + (\eta-2)\dot{\beta}\dot{\gamma}v^2\sin(\gamma) - \eta\dot{\gamma}v^2 p_2(\tau) = \tilde{M}_{y_2} - \tilde{K}_x\sin(\beta) - \tilde{C}_y v\dot{\beta}\cos(\gamma), \tag{20}$$

where the following non-dimensional quantities have been introduced: $v = \Omega/\Omega_0$; $\Omega_0$ being a reference frequency (taken as the first bending frequency of a non-rotating beam pinned at both ends, for facility of comparison with the flexible model). The overdot now stands for $\mathrm{d}/\mathrm{d}\tau$, $\eta = J_{z_2,o}/J$, $J = J_{x_2,o} = J_{y_2,o}$, $p_2(\tau)$ is obtained from equation (6) and $\tilde{K}_x = l^2K_x/(J\Omega_0^2)$, $\tilde{K}_y = l^2K_y/(J\Omega_0^2)$, $\tilde{C}_x = l^2C_x/(J\Omega_0)$, $\tilde{C}_y = l^2C_y/(J\Omega_0)$, $\tilde{M}_{x_2} = M_{x_2}/(J\Omega_0^2)$, $\tilde{M}_{y_2} = M_{y_2}/(J\Omega_0^2)$. $\tilde{M}_{x_2}$ and $\tilde{M}_{y_2}$ are very complicated functions and details are not given. They are handled using MAPLE [20] in the results given later using the non-linear model.

Assuming that the deflections at the bearings are small, one can use small angle approximations. The following linear model is then obtained:

$$
\begin{aligned}
&v^2\begin{Bmatrix}\ddot{\gamma}\\ \ddot{\beta}\end{Bmatrix} + v\begin{bmatrix}\tilde{C}_{y_2} & \eta v p_2(\tau)\\ -\eta v p_2(\tau) & \tilde{C}_{x_2}\end{bmatrix}\begin{Bmatrix}\dot{\gamma}\\ \dot{\beta}\end{Bmatrix} + \begin{bmatrix}\tilde{K}_y & 0\\ 0 & \tilde{K}_x\end{bmatrix}\begin{Bmatrix}\gamma\\ \beta\end{Bmatrix} + \Gamma\begin{bmatrix}0 & 1\\ -1 & 0\end{bmatrix}\begin{Bmatrix}\gamma\\ \beta\end{Bmatrix}\\
&\quad + \Gamma\sin(2\tau)\begin{bmatrix}-1 & 0\\ 0 & 1\end{bmatrix}\begin{Bmatrix}\gamma\\ \beta\end{Bmatrix} + \Gamma\cos(2\tau)\begin{bmatrix}0 & 1\\ 1 & 0\end{bmatrix}\begin{Bmatrix}\gamma\\ \beta\end{Bmatrix}\\
&\quad = \Gamma\begin{bmatrix}\sin(2\tau) & -(1+\cos(2\tau))\\ 1-\cos(2\tau) & -\sin(2\tau)\end{bmatrix}\begin{Bmatrix}\delta_0\\ \alpha_0\end{Bmatrix},
\end{aligned}
\tag{21}
$$

where $\Gamma = T_0/(2J\Omega_0^2)$.

An analysis of these equations reveals the presence of the direct bending moments transmitted by the U-Joint. They appear on the fourth, fifth and sixth terms of the set of equations. The fifth and sixth terms involve time dependent coefficients and can lead to parametric resonances. The fourth term can lead to flutter type instabilities. The right-hand sides of the equations are due to the inclusion of the initial joint angles in the formulation and can lead to forced motion resonances.

The homogeneous parts of equations (21) lead to a model similar to one obtained by Iwatsubo and Saigo [17], if one neglects second order effects such as $\alpha_0^2$, $\delta_0^2$ and $\alpha_0\delta_0$. Iwatsubo and Saigo's model does not contain these second order effects because the fluctuation of the angular velocity of the driven shaft was not taken into account (which is the same as using the approximation $p_2(\tau) = 1$). Moreover, since in their work the initial joint angles are not included, the forcing terms that are present in equations (21) do not appear.

In the sequel the numerical results presented are for the linear model, except where otherwise noted.

## 3. EQUATIONS OF MOTION: FLEXIBLE MODEL

Here the equations of motion are developed with respect to an inertial frame, namely the frame $xyz$ of section 2. This is essentially the "shadow beam" approach, with the $z$-axis directed along the shaft (treated as rigid) axis. The main modelling features are as follows.

The Rayleigh beam theory is used (in the sequel only slender shafts are treated, so shear deformations are taken to be negligible). Elastic transverse deformations $u$ and $v$ of the neutral axis are measured with respect to $xyz$. If the driven shaft were rigid it would rotate at an angular velocity $\omega$ about its axis. In Rayleigh beam theory kinematics, a cross-sectional area disk (disk of thickness $\Delta z$ and cross-sectional area $A$) is treated as rigid. The angular velocity of that disk is taken to be

$$\boldsymbol{\omega}_D = -\frac{\partial^2 v}{\partial z\,\partial t}\hat{\mathbf{i}} + \frac{\partial^2 u}{\partial z\,\partial t}\hat{\mathbf{j}} + \omega\hat{\mathbf{k}}.$$

Axial and torsional displacements are neglected, since the associated frequencies are much higher than the bending frequencies for the examples studied.

A major issue is the treatment of the moment **M** transmitted by the U-Joint to the driven shaft. This moment is known to be along the normal vector to the crosspiece, which in turn depends on the orientation of the driven shaft. If one includes the instantaneous slopes due to deformation at the U-Joint end, one can write ($f$ denotes a functional form; $\alpha_0$ and $\delta_0$ are the initial joint angles)

$$\mathbf{M} = M\mathbf{e}_n = f\left(\alpha_0 + \left.\frac{\partial u}{\partial z}\right|_{z=0}, \delta_0 - \left.\frac{\partial v}{\partial z}\right|_{z=0}\right). \tag{22}$$

Resolving **M** along the $xyz$ axes, leads to two bending moments $M_x$ and $M_y$ and one twisting torque $M_z$. At this juncture several approaches are possible, namely

(1) The slopes $\partial u/\partial z|_{z=0}$, $\partial v/\partial z|_{z=0}$ could be neglected in equation (22). This can be shown to lead to a forced motion problem only. The bending moments would not cause any parametric instabilities.

(2) The torque could be treated as acting along the deformed configuration (as done by Rosenberg [16]), with the bending moments handled as described in (1). It was found that this approach led only to weak parametric instabilities. Since the parametric instabilities in an actual laboratory model (specifications given later) were quite strong, this approach was abandoned.

(3) The deformation slopes in equation (22) are retained. This, as the sequel will show, leads to the physically observed feature of strong parametric resonances. Thus, approach (3) is used. Also, following Rosenberg's work, the torque was taken to act along the deformed configuration. Note that the bending moments are incorporated into the model by treating them as point couples acting at the U-Joint, handled mathematically by Dirac delta functions.

Less problematical modelling features are: the springs (bearings) are treated by the appropriate choice of Galerkin functions; the dampers (bearings) are modelled as linear viscous dampers, treated as point forces handled mathematically by Dirac delta functions.

With the above assumptions the non-dimensional equations of motion can be shown to be (see reference [19]):

$$EI\frac{\partial^4 u}{\partial z^4} + \rho A\frac{\partial^2 u}{\partial t^2} + F_{d_x} + \frac{\partial M_{b_y}}{\partial z} + T\frac{\partial^3 v}{\partial z^3} = \frac{1}{4}\rho A R^2\left(\frac{\partial^4 u}{\partial z^2\,\partial t^2} + 2\omega\frac{\partial^3 v}{\partial z^2\,\partial t}\right), \tag{23}$$

$$EI\frac{\partial^4 v}{\partial z^4} + \rho A\frac{\partial^2 v}{\partial t^2} + F_{d_y} - \frac{\partial M_{b_x}}{\partial z} - T\frac{\partial^3 u}{\partial z^3} = \frac{1}{4}\rho A R^2\left(\frac{\partial^4 v}{\partial z^2\,\partial t^2} - 2\omega\frac{\partial^3 u}{\partial z^2\,\partial t}\right), \tag{24}$$

where $F_{d_x}$, $F_{d_y}$ are external damping forces per unit length, $M_{b_x}$ and $M_{b_y}$ are external bending moments per unit length, $\omega$ is the angular velocity of the driven shaft (treated as rigid) and is given by equation (6). Also, $E$ denotes Young's modulus,

$I$ the area moment of inertia, $\rho$ the mass density, $A$ the cross-sectional area and $R$ the cross-sectional radius.

These equations are subjected to the boundary conditions

$$u = v = u'' = v'' = 0, \qquad z = 0; \qquad u'' = v'' = 0, \qquad z = l;$$
$$EIu''' = K_x u, \qquad z = l; \qquad EIv''' = K_y v, \qquad z = l. \tag{25}$$

The bending moments transmitted by the U-Joint are given by

$$M_x = \frac{T_0}{2}\left[\left(\delta_0 - \left.\frac{\partial v}{\partial z}\right|_{z=0}\right)\sin(2\Omega t) - \left(\alpha_0 + \left.\frac{\partial u}{\partial z}\right|_{z=0}\right)(1 + \cos(2\Omega t))\right], \tag{26}$$

$$M_y = \frac{T_0}{2}\left[\left(\delta_0 - \left.\frac{\partial v}{\partial z}\right|_{z=0}\right)(1 - \cos(2\Omega t) - \left(\alpha_0 + \left.\frac{\partial u}{\partial z}\right|_{z=0}\right)\sin(2\Omega t))\right]. \tag{27}$$

Consequently,

$$M_{b_x} = M_x \Delta(z), \qquad M_{b_y} = M_y \Delta(z),$$

where $\Delta$ stands for the Dirac delta function.

The transmitted torque is given by (the magnitude is taken to be constant along the shaft)

$$T = T_0 p_1(t) = T_0\left[1 + \frac{\alpha_0^2}{2}(1 - \cos(2\Omega t)) + \frac{\delta_0^2}{2}(1 + \cos(2\Omega t)) + \alpha_0\delta_0 \sin(2\Omega t)\right]. \tag{28}$$

Also

$$F_{d_x} = C_x \left.\frac{\partial u}{\partial t}\right|_{z=l} \Delta(z - l), \qquad F_{d_y} = C_y \left.\frac{\partial v}{\partial t}\right|_{z=l} \Delta(z - l).$$

Introducing the dimensionless variables and parameters: $U = u/l$, $V = v/l$, $Z = z/l$, $\Lambda(Z) = l\Delta(z)$, $\nu = \Omega/\Omega_0$, $\Omega_0 = (\pi^2/l^2)\sqrt{EI/(\rho A)}$ (the lowest bending frequency of a non-rotating pinned–pinned Euler–Bernoulli beam), $\Gamma_1 = T_0/(\rho A \Omega_0^2 l^3)$, $X_2 = EI/(\rho A \Omega_0^2 l^4)$, $X_3 = R^2/(4l^2)$, $X_4 = 2X_3$, $d_1 = C_x/(\rho A \Omega_0 l)$, $d_2 = C_y/(\rho A \Omega_0 l)$, then, using equations (26), (27) and (28), equations (23) and (24) become

$$X_2 \frac{\partial^4 U}{\partial Z^4} + \nu^2 \frac{\partial^2 U}{\partial \tau^2} + d_1 \nu \left.\frac{\partial U}{\partial \tau}\right|_{Z=1} \Lambda(Z - 1) + \Gamma_1 \frac{\partial^3 V}{\partial Z^3} p_1(\tau) - X_3 \nu^2 \frac{\partial^4 U}{\partial Z^2\, \partial \tau^2}$$
$$- X_4 \nu^2 p_2(\tau) \frac{\partial^3 V}{\partial Z^2\, \partial \tau} - \frac{\Gamma_1}{2}\left.\frac{\partial V}{\partial Z}\right|_{Z=0} (1 - \cos(2\tau)) \frac{\mathrm{d}(\Lambda(Z))}{\mathrm{d}Z} - \frac{\Gamma_1}{2}\left.\frac{\partial U}{\partial Z}\right|_{Z=0}$$
$$\times \sin(2\tau) \frac{\mathrm{d}(\Lambda(Z))}{\mathrm{d}Z} = \frac{\Gamma_1}{2}\frac{\mathrm{d}(\Lambda(Z))}{\mathrm{d}Z}[\alpha_0 \sin(2\tau) - \delta_0(1 - \cos(2\tau))], \tag{29}$$

$$X_2\frac{\partial^4 V}{\partial Z^4}+v^2\frac{\partial^2 V}{\partial \tau^2}+d_2 v\frac{\partial V}{\partial \tau}\bigg|_{Z=1}\Lambda(Z-1)-\Gamma_1\frac{\partial^3 U}{\partial Z^3}p_1(\tau)-X_3v^2\frac{\partial^4 V}{\partial Z^2\,\partial\tau^2}$$

$$+X_4v^2p_2(\tau)\frac{\partial^3 U}{\partial Z^2\,\partial\tau}+\frac{\Gamma_1}{2}\frac{\partial U}{\partial Z}\bigg|_{Z=0}(1+\cos(2\tau))\frac{\mathrm{d}(\Lambda(Z))}{\mathrm{d}Z}+\frac{\Gamma_1}{2}\frac{\partial V}{\partial Z}\bigg|_{Z=0}$$

$$\times\sin(2\tau)\frac{\mathrm{d}(\Lambda(Z))}{\mathrm{d}Z}=\frac{\Gamma_1}{2}\frac{\mathrm{d}(\Lambda(Z))}{\mathrm{d}Z}[\delta_0\sin(2\tau)-\alpha_0(1+\cos(2\tau))]. \tag{30}$$

## 4. GALERKIN'S METHOD

The solutions are assumed to have the following form

$$U=\sum_{i=1}^{\infty}\Phi_i(Z)F_i(\tau),\qquad V=\sum_{i=1}^{\infty}\Psi_i(Z)G_i(\tau).$$

Application of Galerkin's method leads to

$$v^2\begin{bmatrix}[\gamma_{1_{mi}}]-X_3[\lambda_{1_{mi}}] & [0]\\ [0] & [\gamma_{2_{mi}}]-X_3[\lambda_{2_{mi}}]\end{bmatrix}\begin{Bmatrix}\{\ddot{F}_i\}\\ \{\ddot{G}_i\}\end{Bmatrix}$$

$$+v\begin{bmatrix}d_1[\xi_{1_{mi}}] & -vp_2(\tau)X_4[\lambda_{3_{mi}}]\\ vp_2(\tau)X_4[\lambda_{4_{mi}}] & d_2[\xi_{2_{mi}}]\end{bmatrix}\begin{Bmatrix}\{\dot{F}_i\}\\ \{\dot{G}_i\}\end{Bmatrix}$$

$$+\begin{bmatrix}X_2[\alpha_{1_{mi}}] & [0]\\ [0] & X_2[\alpha_{2_{mi}}]\end{bmatrix}\begin{Bmatrix}\{F_i\}\\ \{G_i\}\end{Bmatrix}$$

$$+\Gamma_1\begin{bmatrix}[0] & [\delta_{3_{mi}}]+p_1(\tau)[\beta_{1_{mi}}]\\ -[\delta_{2_{mi}}]-p_1(\tau)[\beta_{2_{mi}}] & [0]\end{bmatrix}\begin{Bmatrix}\{F_i\}\\ \{G_i\}\end{Bmatrix}$$

$$+\Gamma_1\sin(2\tau)\begin{bmatrix}[\delta_{1_{mi}}] & [0]\\ [0] & -[\delta_{4_{mi}}]\end{bmatrix}\begin{Bmatrix}\{F_i\}\\ \{G_i\}\end{Bmatrix}$$

$$+\Gamma_1\cos(2\tau)\begin{bmatrix}[0] & -[\delta_{3_{mi}}]\\ -[\delta_{2_{mi}}] & [0]\end{bmatrix}\begin{Bmatrix}\{F_i\}\\ \{G_i\}\end{Bmatrix}$$

$$=\begin{Bmatrix}\dfrac{\Gamma_1}{2}(\delta_0(1-\cos(2\tau))-\alpha_0\sin(2\tau))\{\Phi'_m(0)\}\\ \dfrac{\Gamma_1}{2}(\alpha_0(1+\cos(2\tau))-\delta_0\sin(2\tau))\{\Psi'_m(0)\}\end{Bmatrix},$$

$$i=1,2,3,\ldots,\infty,\quad m=1,2,3,\ldots,\infty. \tag{31}$$

The coefficients in the above equations are listed in Appendix A.

The first matrix on the left-hand side of equation (31) is the "mass" matrix and has constant coefficients. The second matrix is due to the damping in the system (main diagonal terms) and to gyroscopic effects (cross diagonal terms). As evidenced by the presence of $p_2(\tau)$, each gyroscopic term has a constant part plus a part that is a function of time. The third matrix is the "stiffness" matrix and has constant coefficients. The fourth matrix has constant and time dependent elements. The time dependent coefficients are contained in the term $p_1(\tau)$ (see equation (28)) and are second order effects. The constant parts of these elements are due to the constant parts of the bending moments from the U-Joint and the follower torque. This matrix can lead to flutter type instabilities and to parametric instabilities (due to $p_1(\tau)$). The fifth and sixth matrices of equation (31) are functions of time. These terms can lead to strong parametric resonances (as will emerge). The forcing term on the right-hand side of equation (31) is due to the inclusion of the initial joint angles ($\alpha_0$ and $\delta_0$) in the formulation and can lead to forced motion type resonances.

The choice of Galerkin functions will now be discussed. Recall that the damping forces and the moments applied by the U-Joint do not arise in the boundary conditions. They are incorporated in the equations of motion via Dirac delta functions. However, as seen in equation (25), the spring forces do arise in the boundary conditions. Consequently, the Galerkin functions chosen are the mode shapes of a non-rotating Euler–Bernoulli beam pinned at one end and spring supported at the other end. Thus, the functions for the *xz* and *yz* planes are, respectively,

$$\Phi_i(Z) = \sinh(H_{(x)i}Z) + \frac{\sinh(H_{(x)i})}{\sin(H_{(x)i})}\sin(H_{(x)i}Z), \tag{32}$$

$$\Psi_i(Z) = \sinh(H_{(y)i}Z) + \frac{\sinh(H_{(y)i})}{\sin(H_{(y)i})}\sin(H_{(y)i}Z), \tag{33}$$

where $H_{(x)i}$ and $H_{(y)i}$ are the positive solutions of the following transcendental equation:

$$H^3[\tan(H) - \tanh(H)] - 2\frac{KL^3}{EI}\tanh(H)\tan(H) = 0, \tag{34}$$

for $K = K_x$ and $K = K_y$, respectively. Note that these Galerkin functions satisfy all the conditions (25).

The Galerkin coefficients involve integrals containing products of hyperbolic functions and are calculated by a MAPLE routine for a given value of $N$ (the series truncation value). Direct use of equations (32) and (33) led to numerical problems in MAPLE because of excessively large values of the integrands. This problem was resolved by using a set of normalized functions:

$$\Phi_i^*(Z) = \frac{\Phi_i(Z)}{\Phi_i(Z)|_{Z=1}}, \qquad \Psi_i^*(Z) = \frac{\Psi_i(Z)}{\Psi_i(Z)|_{Z=1}}.$$

## 5. FLUTTER INSTABILITIES

Neglecting the time dependent coefficients and using the approximation $p_2 \cong 1$ (since $\alpha_0$ and $\delta_0$ are small), the homogeneous part of equation (21), for the rigid body model, reduces to

$$v^2\begin{Bmatrix}\ddot{\gamma}\\ \ddot{\beta}\end{Bmatrix} + v\begin{bmatrix}\tilde{C}_{y_2} & \eta v\\ -\eta v & \tilde{C}_{x_2}\end{bmatrix}\begin{Bmatrix}\dot{\gamma}\\ \dot{\beta}\end{Bmatrix} + \begin{bmatrix}\tilde{K}_y & \Gamma\\ -\Gamma & \tilde{K}_x\end{bmatrix}\begin{Bmatrix}\gamma\\ \beta\end{Bmatrix} = \begin{Bmatrix}0\\ 0\end{Bmatrix}. \tag{35}$$

Similarly, for the flexible model, the homogeneous part of equation (31) reduces to

$$v^2[\tilde{M}]\{\ddot{\tilde{Q}}\} + v[\tilde{D}]\{\dot{\tilde{Q}}\} + [\tilde{S}]\{\tilde{Q}\} = \{0\}, \tag{36}$$

where

$$[\tilde{M}] = \begin{bmatrix}[\gamma_{1_{mi}}] - X_3[\lambda_{1_{mi}}] & [0]\\ [0] & [\gamma_{2_{mi}}] - X_3[\lambda_{2_{mi}}]\end{bmatrix}, \quad [\tilde{D}] = \begin{bmatrix}d_1[\xi_{1_{mi}}] & -vX_4[\lambda_{3_{mi}}]\\ vX_4[\lambda_{4_{mi}}] & d_2[\xi_{2_{mi}}]\end{bmatrix},$$

$$[\tilde{S}] = \begin{bmatrix}X_2[\alpha_{1_{mi}}] & \Gamma_1[\delta_{3_{mi}}] + \Gamma_1[\beta_{1_{mi}}]\\ -\Gamma_1[\delta_{2_{mi}}] - \Gamma_1[\beta_{2_{mi}}] & X_2[\alpha_{2_{mi}}]\end{bmatrix}, \qquad \{\tilde{Q}\} = \begin{Bmatrix}\{F_i\}\\ \{G_i\}\end{Bmatrix}. \tag{37}$$

Both equations (35) and (36) are approximate equations which permit fairly simple, non-computationally intensive methods to be employed for exploring flutter instabilities. It will be shown later that the results so obtained are highly accurate, as seen by comparisons with the results obtained by the monodromy matrix method, which is exact.

Flutter instabilities occur whenever the associated eigenvalues of equations (35) or (36) have a positive real part.

During some numerical simulations it was discovered that both systems are unstable for all values of rotational speed and torque if the damping is zero. This is a rather alarming result at first glance but, as will be shown shortly, it is of no practical consequence. Note that this also occurs in the model developed by Iwatsubo and Saigo [17].

The instability for $C = 0$ can be readily seen in the case $\tilde{C}_x = \tilde{C}_y = \tilde{C}$ and $\tilde{K}_x = \tilde{K}_y = \tilde{K}$. For the rigid body case, taking solutions of the form

$$\gamma = \gamma_0\,\mathrm{e}^{\lambda\tau}, \qquad \beta = \beta_0\,\mathrm{e}^{\lambda\tau},$$

equation (35) leads to a root for $\lambda$:

$$\lambda = \frac{1}{2v}\left[-\tilde{C} + \eta v I + \sqrt{(\tilde{C}^2 - v^2\eta^2 - 4\tilde{K}) + (4\Gamma - 2\tilde{C}v\eta)I}\right]$$

where $I = \sqrt{-1}$. When $\tilde{C} = 0$, the real part of this complex number is always positive and so the system is unstable in the entire parameter space of $v$ and $\Gamma$.

Consider now the case where $\tilde{C} \neq 0$. A numerical illustration will be given, hereafter referred to as the "laboratory model" (the terminology is based on an actual model that was built). The parameter values are $\alpha_0 = \delta_0 = 10^\circ$,

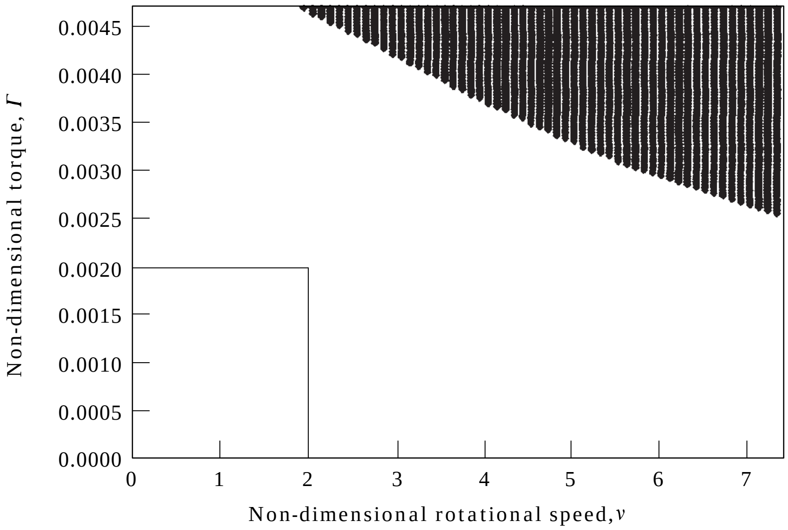

Figure 3. Flutter instability: rigid body laboratory model.

$l = 4{\cdot}6 \times 10^{-1}$ m, $E = 2{\cdot}07 \times 10^{11}$ N/m$^2$, $\rho = 7{\cdot}83 \times 10^3$ kg/m$^3$, $R = 2{\cdot}40 \times 10^{-3}$ m, $\eta = 3{\cdot}96 \times 10^{-5}$, $I = 2{\cdot}53 \times 10^{-11}$ m$^4$ $(I_{xx} = I_{yy} = I = \pi R^4/4)$, $K_x = 25{\cdot}17$ N/m and $K_y = 7{\cdot}74$ N/m. For this model a value of $C_x = C_y = 1 \times 10^{-3}$ N/(m/s) was assumed. By direct numerical integration of equation (35), subjected to some initial conditions, a logarithmic decrement procedure led to $\zeta_1 \approx \zeta_2 = 0{\cdot}001$ ($\zeta_1$, $\zeta_2$ are the non-dimensional damping ratios associated with $\gamma$ and $\beta$, respectively).

Shown in Figures 3 and 4 are plots of the flutter instability zones for the rigid and flexible models (three terms were used in the Galerkin approximation,

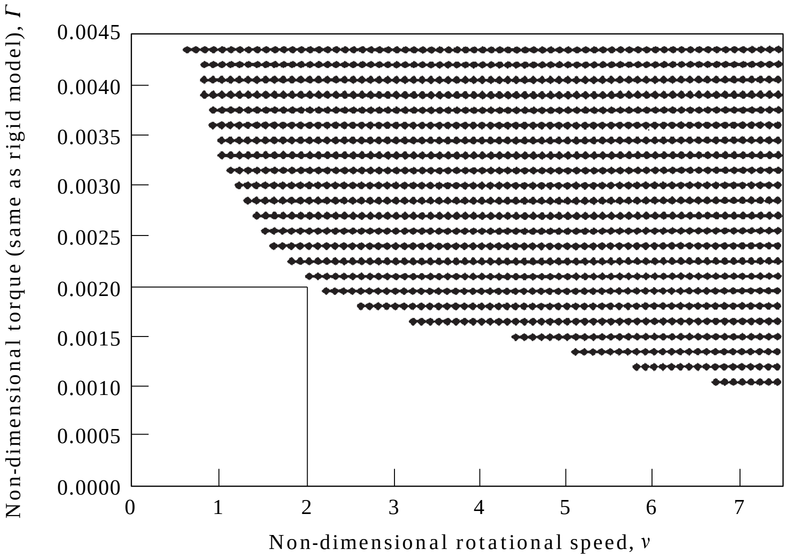

Figure 4. Flutter instability: flexible laboratory model.

sufficient for convergence) in torque-rotational speed space. Limits of practical operation are also shown as boxes in the lower left-hand corners of Figures 3 and 4. The maximum attainable rotational speed of the laboratory model is judged to be 5000 rpm, which gives $\nu = 2{\cdot}0$. The value (non-dimensional) of the statically applied torque which would cause the shaft to yield (static yielding) is $\Gamma = 0{\cdot}0042$. The static torque which would cause a $10^\circ$ angle of twist is $\Gamma = 0{\cdot}0021$ and this is chosen as the limit of the practical torque range.

The main conclusion to be drawn is that the very light damping used moves the flutter instability zones outside the range of practical operation for both models. Similar results were found for other sets of parameter values.

## 6. PARAMETRIC INSTABILITIES

When the forcing terms are neglected, equations (21) and (31) are sets of Mathieu–Hill equations. Several approaches for the determination of the regions of parametric instability of such equations exist in the literature.

Throughout this work the regions of instability are obtained by a numerical technique based on the so-called monodromy matrix (see reference [21]). The monodromy matrix technique is very computationally intensive, but offers some advantages over perturbation techniques and Hill's infinite determinant. For instance, the method does not involve any approximations and is able to capture all instabilities within a parameter range (to within numerical accuracy).

Very briefly put, the technique is as follows. The equations of motion are cast into a first order form:

$$\{\dot{q}(t)\} = [A(t)]\{q(t)\}, \tag{38}$$

where the matrix $[A(t)]$ is $T^*$-periodic. The fundamental matrix is denoted by

$$[\Theta(T^*)] = [\{q_1(T^*)\}, \{q_2(T^*)\}, \dots, \{q_n(T^*)\}],$$

where $\{q_1(t)\}, \{q_2(t)\}, \dots, \{q_n(t)\}$ are any $n$ linearly independent solutions of the system. Integrating equation (38) $n$ times from 0 to $T^*$ with the $n$ initial conditions

$$[\Theta(0)] = \begin{bmatrix} 1 & 0 & \cdots & 0 \\ 0 & 1 & \cdots & 0 \\ \vdots & \vdots & \ddots & \vdots \\ 0 & 0 & \cdots & 1 \end{bmatrix} = [I]$$

generates a matrix $[S]$, the monodromy matrix, given by $[S] = [\Theta(T^*)]$. Then the eigenvalues of $[S]$, $\sigma_j$, are determined. The system is stable when $\|\sigma_j\| \leqslant 1$, $j = 1, 2, \dots, n$. The process is repeated for every pair of $\nu$ and $\Gamma$ to cover the entire parameter space of interest.

In the zero damping case, parametric resonances are expected to emanate at zero torque ($\Gamma = 0$), from (so-called principal zones)

$$\nu = \frac{\nu_{n_i}}{j}, \qquad i = 1, 2, 3 \dots, \qquad j = 1, 2, 3 \dots, \tag{39}$$

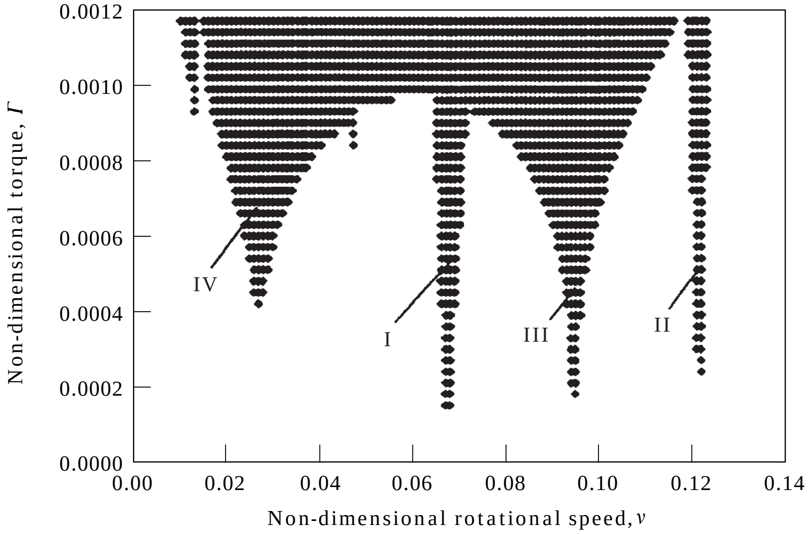

Figure 5. Parametric instability: rigid body laboratory model.

where the $\nu_{n_i}$'s are the non-dimensional natural frequencies of the rotating shaft ($\nu_n = \Omega_n/\Omega_0$, the $\Omega_n$ being the natural frequencies of the rotating shaft).

Combination parametric resonances may also occur. These emanate, at $\Gamma = 0$, from the points (for zero damping)

$$\nu = \left|\frac{\nu_{n_i} \pm \nu_{n_j}}{2k}\right|, \qquad i = 1, 2, 3 \ldots, \qquad j = 1, 2, 3 \ldots, \qquad k = 1, 2, 3 \ldots. \quad (40)$$

Note that damping will shift the points of emanation to values of $\Gamma > 0$.

In general, the rigid body model has two natural frequencies; these correspond to the shaft bouncing on the springs in two planes. These frequencies are functions of the shaft's rotational speed. Specifically, one frequency increases with the rotational speed and is called the forward precessional frequency, and the second decreases with the rotational speed and is called the backward precessional frequency. Note that for the examples treated here the difference between the rotating and non-rotating frequencies is negligible. In the flexible model the frequencies will also be influenced by rotation but, again, the differences were found to be negligible. The first two modes of the flexible system are nearly identical to the rigid body modes since the spring stiffness is very small compared to the shaft stiffness. These two modes will be referred to as "predominantly rigid modes". The additional frequencies stem from the flexibility of the shaft.

For the flexible model, convergence was checked by comparing corresponding zones of instability obtained by using increasing numbers of Galerkin functions. In all results convergence was achieved by using less than four Galerkin functions.

As a first example consider the laboratory model treated previously in section 5. The natural frequencies corresponding to predominantly rigid modes for this system are $\nu_{n_1} = 0{\cdot}067$ and $\nu_{n_2} = 0{\cdot}121$. The first two natural frequencies associated with shaft flexibility for this system are $\nu_{n_3} = 1{\cdot}564$ and $\nu_{n_4} = 1{\cdot}569$. Figures 5 and

6 give plots of the instability zones (hashed zones indicate instability) as functions of non-dimensional torque $\Gamma$ and non-dimensional rotational speed $\nu$ for the rigid body model and for the flexible model, respectively (in Figure 6 the zones of instability corresponding to the shaft flexibility are off scale). In the figures, zones I and II are principal zones emanating from $\nu_{n_1} = 0{\cdot}067$ and $\nu_{n_2} = 0{\cdot}121$, respectively, and zones III and IV are combination zones emanating from $(\nu_{n_1} + \nu_{n_2})/2 = 0{\cdot}094$ (III) and $(\nu_{n_2} - \nu_{n_1})/2 = 0{\cdot}027$ (IV). Note that the values of $\nu$ and $\Gamma$ are within practical range. On the plots the rotational speeds range from, approximately, $\nu = 0{\cdot}02$ to $0{\cdot}14$ (54 to 376 rpm). The largest value of torque shown is $\Gamma = 0{\cdot}0012$ (0·84 Nm, which is approximately 29% of the value required for yielding).

It is seen that there is an excellent agreement between the zones predicted by the two different models and so shaft flexibility does not influence the rigid instability zones in this case. This is not surprising since the "rigid" frequencies and "flexible" frequencies differ significantly. It is anticipated that flexibility will only influence the "rigid" zones when the rigid and flexible natural frequencies are close.

Note that the width of the zones is significant. For example, for a torque $\Gamma = 0{\cdot}0008$ (19% of the yield torque) the shaft will cross four zones of instability. These are zone IV (about 47 rpm or 65% of the operating speed), zone I (about 18 rpm or 10% of the operating speed), zone III (about 54 rpm or 21% of the operating speed) and zone II (about 11 rpm or 3·4% of the operating speed). Note further that increasing the torque increases the width of the zones, thus destabilizing the sytem.

Figures 7 and 8 give plots of instability zones for the flexible model for larger values of rotational speed. It is seen that new zones arise, namely, zones V, VI, VII, VIII (combination zones between predominantly rigid and flexible modes)

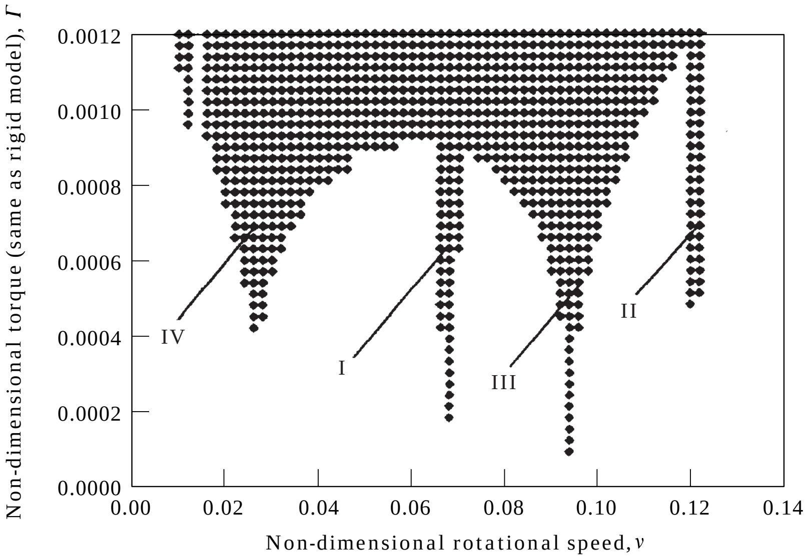

Figure 6. Parametric instability: flexible laboratory model.

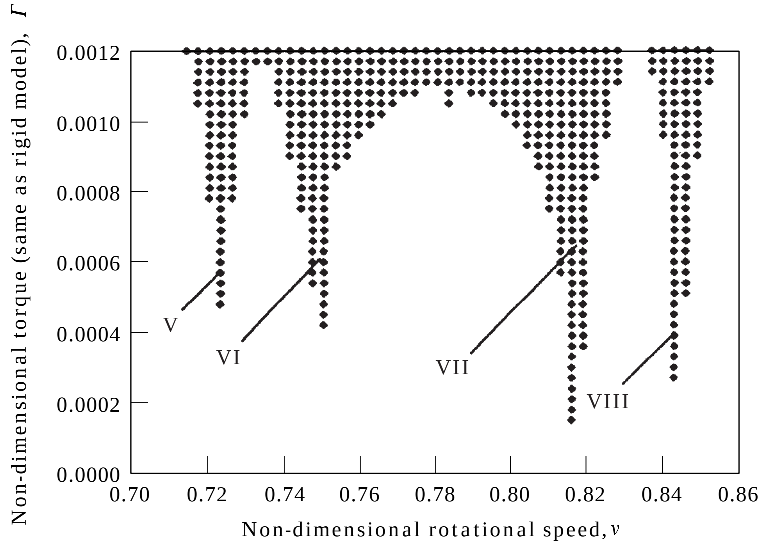

Figure 7. Parametric instability: flexible laboratory model.

and IX, X (principal zones due to flexibility; some overlapping is seen). All the new zones occur within a practical range of rotational speed and torque. Thus, flexibility of the shaft can lead to zones of possible practical interest.

Note that the monodromy matrix technique also captures flutter instabilities but they are off scale in the figures shown.

Some effects of damping will now be addressed. Figure 9 gives the instability zones when the damping is increased to $\zeta = 0{\cdot}01$ ($\zeta \equiv \zeta_1 \approx \zeta_2$). Comparing this figure with Figure 6 shows that an increase in damping has a stabilizing effect in the system. Combination zone IV (difference type) disappears and combination zone III (sum type) is severely reduced. The principal zones I and II, due to

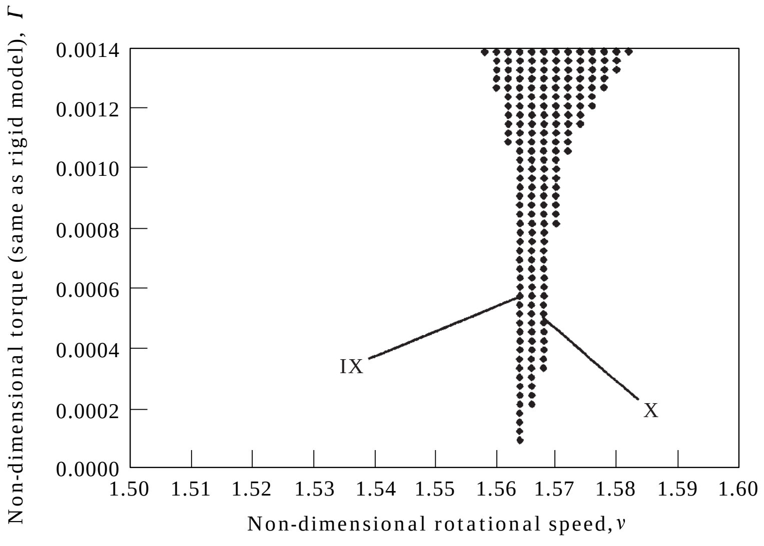

Figure 8. Parametric instability: flexible laboratory model.

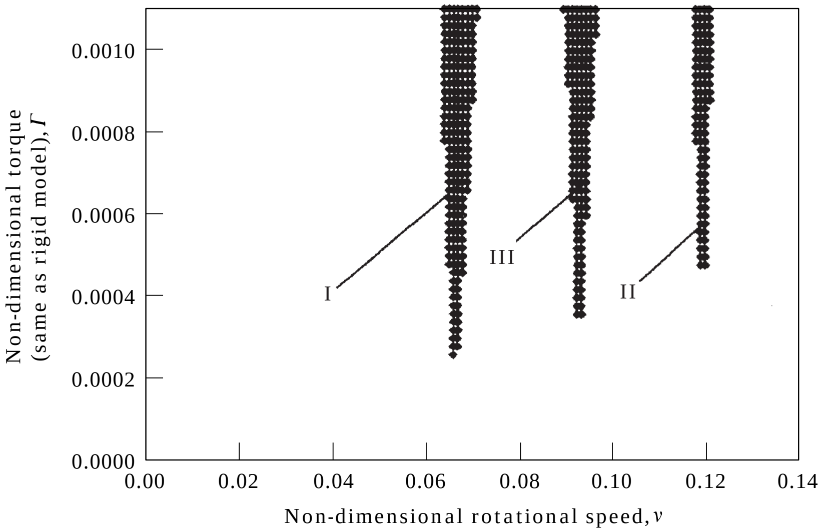

Figure 9. Parametric instability: flexible laboratory model (damping ratio = 0·01).

predominantly rigid modes, are not severely affected. The same conclusions were found for the corresponding zones in the rigid body model.

Figures 10 and 11 show the effect of higher damping on the new zones given by shaft flexibility. On comparing Figure 10 to Figure 7 it is seen that some combination zones are pushed out of the range of operation (V and VI—difference type) and some remain inside the range (VII and VIII—sum type). The flexible zones, which remained inside the range of operation, had their width reduced but are sufficiently wide to be of possible practical concern. On comparing Figure 11 to Figure 8 it is seen that the principal zones IX and X are affected by the increase

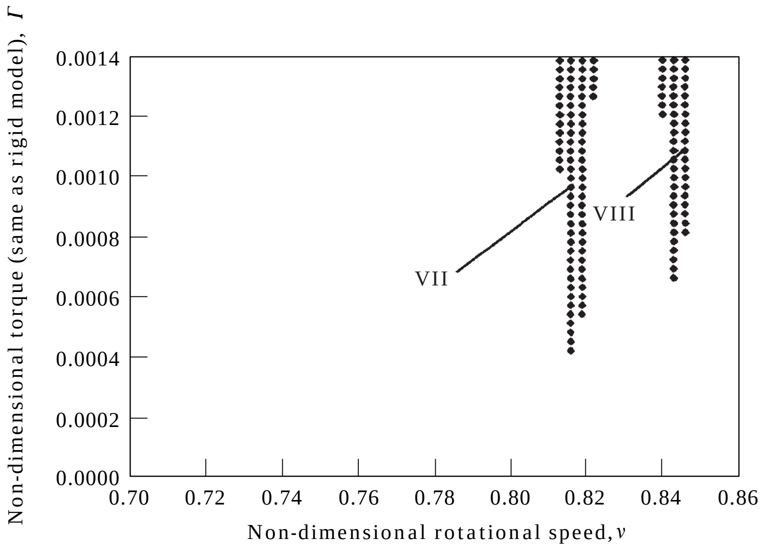

Figure 10. Parametric instability: flexible laboratory model (damping ratio = 0·01).

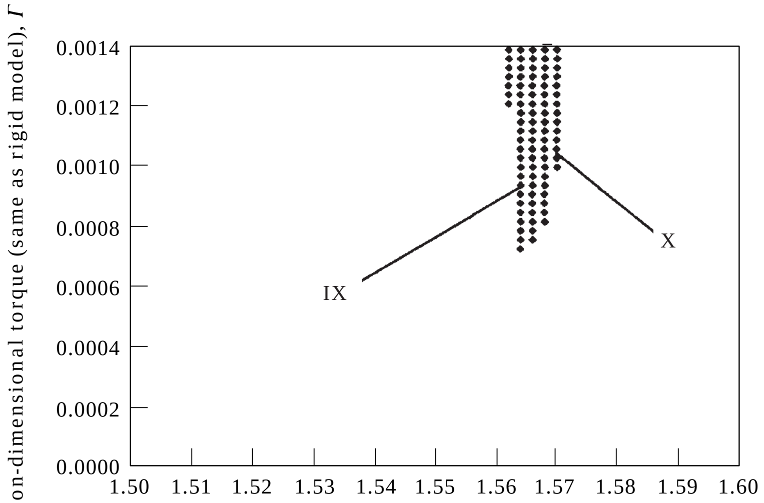

Figure 11. Parametric instability: flexible laboratory model (damping ratio = 0·01).

in damping, but are still sufficiently robust to be also of possible practical concern.

Some results for a second example (a hollow shaft of automotive proportions) will now be given. The following parameters are used: $l = 8{\cdot}96 \times 10^{-1}$ m, $\rho = 7{\cdot}83 \times 10^{3}$ kg/m$^3$, $E = 2{\cdot}07 \times 10^{11}$ N/m$^2$, $R_o = 3{\cdot}4950 \times 10^{-2}$ m (outer radius), $R_i = 3{\cdot}3300 \times 10^{-2}$ m (inner radius) and $\eta = 4{\cdot}5542 \times 10^{-3}$. The spring rates are $K_x = 2{\cdot}50 \times 10^{3}$ N/m and $K_y = 1{\cdot}06 \times 10^{4}$ N/m. Small and moderate values of the damping coefficients will be assumed and significant differences/trends, if any, noted and analyzed. The damping coefficients will initially be taken as

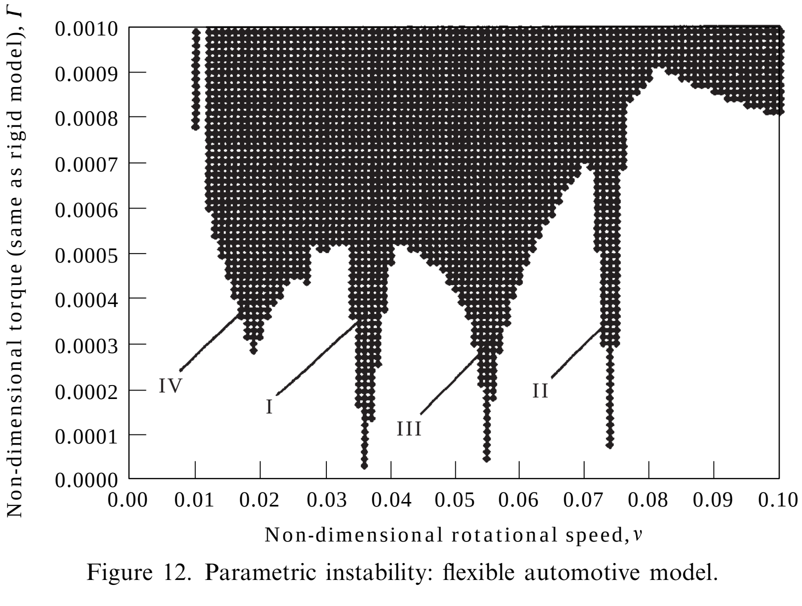

Figure 12. Parametric instability: flexible automotive model.

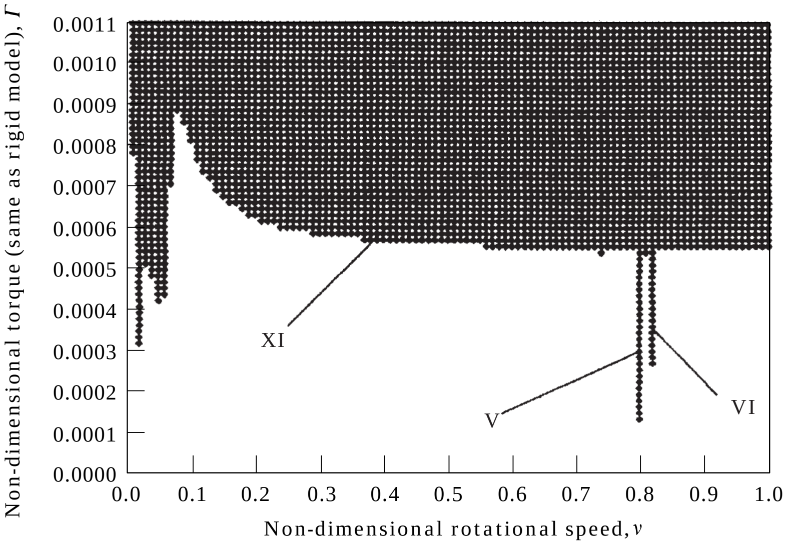

Figure 13. Dynamic instability: flexible automotive model.

$C_x = C_y = 5{\cdot}0 \times 10^{-1}$ N/(m/s). The corresponding damping ratios are approximately $\zeta_1 = 0{\cdot}007$ and $\zeta_2 = 0{\cdot}003$.

For this shaft static yielding will occur when the torque reaches approximately $1{\cdot}7 \times 10^3$ Nm ($\Gamma = 0{\cdot}0005$). The first four non-dimensional natural frequencies for this system are: $\nu_{n_1} = 0{\cdot}036$, $\nu_{n_2} = 0{\cdot}074$ (predominantly rigid body modes), $\nu_{n_3} = 1{\cdot}563$ and $\nu_{n_4} = 1{\cdot}565$ (flexible modes).

Figure 12 shows the zones of parametric instabilities, given by the flexible model, for this system. Note the principal zones I ($\nu_{n_1}$) and II ($\nu_{n_2}$) and the combination zones III ($(\nu_{n_1} + \nu_{n_2})/2$) and IV ($(\nu_{n_2} - \nu_{n_1})/2$). As in the laboratory model example, it is seen that the width of the zones can be of practical concern. For example, for rotational speeds ranging from 0 to 1500 rpm and for a level of torque around 40% of the torque necessary to cause static yielding of the shaft ($\Gamma = 0{\cdot}0002$), the system will cross three zones of instability. These are: zone I (width of 101 rpm, roughly 18% of operating speed), zone III (width of 76 rpm, 9% of operating speed) and zone II (width of 25 rpm, 2% of operating speed).

Note also that, as in the previous example, an increase in torque leads to an increase in the width of the zones (destabilizing effect on the system).

A comparison between Figure 12 and corresponding results using the rigid body model revealed, as in the laboratory case, no significant differences.

Figure 13 shows the dynamic instabilities for a wider range of rotational speed (0→14 500 rpm). Note that there is a zone of flutter instability (denoted by XI) now appearing, but outside the practical range of operation. It is interesting to see that the monodromy matrix technique captures the flutter instabilities. At this stage it seems appropriate to note that the flutter zones determined by the approximation of omitting the time dependent coefficients (see section 5) turned out to be highly accurate. Therefore, the approximation gives a reliable and simple way for calculating the flutter zones.

In addition to the predominantly rigid modes zones, Figure 13 shows two combination zones between flexible and rigid modes, namely, zone V ($(\nu_{n_3} + \nu_{n_1})/2$) and zone VI ($(\nu_{n_4} + \nu_{n_2})/2$). In contrast to the laboratory model, here these combination zones are not of practical importance. The reason for that is the value of the rotational speed for which they occur. These speeds are close to 11 650 rpm ($\nu \cong 0{\cdot}8$) which is not practical for this system. Consequently, the parametric instabilities of practical concern here are due to the predominantly rigid modes only, in contrast to the laboratory model. Figure 13 does not include the instability zones due to flexibility since these occur at unreasonable values of rotational speed. Pure flexible zones are not important for the automotive shaft model, again in contrast to the laboratory model.

In summary the automotive shaft, either using the rigid body model or the flexible model, exhibits parametric instabilities under normal conditions of operation.

Possible design changes that would eliminate the possibility of instabilities in the shaft will be addressed. A modification that will change the instabilities of the system is an increase in bearing damping. Higher damping will cause the zones of parametric instability to begin at higher values of torque and will also lead to thinner zones. Thus, it is possible to calculate a value of damping that will move the zones outside the range of practical torque. Figure 14 shows the parametric instability zones when the damping is increased by a factor of ten ($C_x = C_y = 5{\cdot}0$ N/(m/s), or $\zeta_1 = 0{\cdot}07$ and $\zeta_2 = 0{\cdot}03$; light to moderate damping). It can be seen that instability zones only occur for values of torque that are larger than the shaft static yielding torque ($\Gamma = 0{\cdot}0005$). Therefore, if such damping could be realized, the shaft would not undergo any instability in the practical range of operation. Note that increasing bearing stiffness could drive the zones of

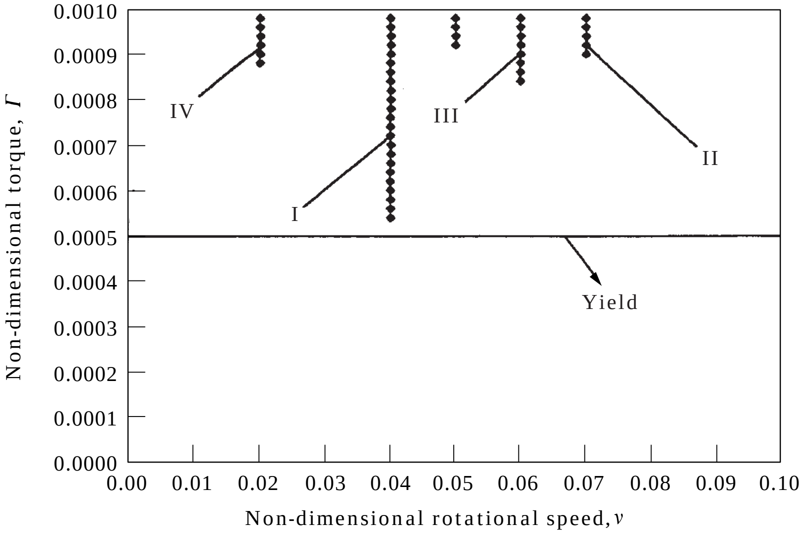

Figure 14. Parametric instability: flexible automotive model ($C_x = C_y = 5{\cdot}0$ N/(m/s)).

parametric instability outside the range of practical rotational speeds. However, the necessary increase in stiffness was found to be impractical.

## 7. NON-LINEAR MODEL

To conclude the work on instabilities of the homogeneous system, some results using the non-linear rigid body model will now be presented. These results were obtained using direct numerical integration of the equations of motion, subjected to non-zero initial conditions. The laboratory model was employed in all cases.

One question that could be raised is whether the fact that flutter instabilities exist in the entire parameter space of $v$ and $\Gamma$, for $C = 0$, is due to the linearization of the model. The answer was found to be no. The non-linear model, for the parameter values studied, also led to flutter instabilities everywhere for zero damping.

Another issue is whether for $C \neq 0$, the non-linear model would move the flutter instability zones into regions of practical significance. The answer was found to be no. Consider the example illustrated in Figure 3. Taking a point just inside and just outside the boundary given there leads to the same conclusions as before.

Consider now the parameter values $\Gamma = 0{\cdot}0002$ and $v = 0{\cdot}067$. These values yield a parametric instability and the linear model yields unbounded growth. The response using the non-linear model is shown in Figure 15. The motion is not unbounded. A finite amplitude is seen. However, this amplitude is approximately 43° and so, from a practical point of view, one could regard the system as being unstable.

Cartmell [22] showed in a model problem that non-linear models could have unbounded as well as bounded solutions. So far, numerical integrations have failed to show unbounded motions for the current model.

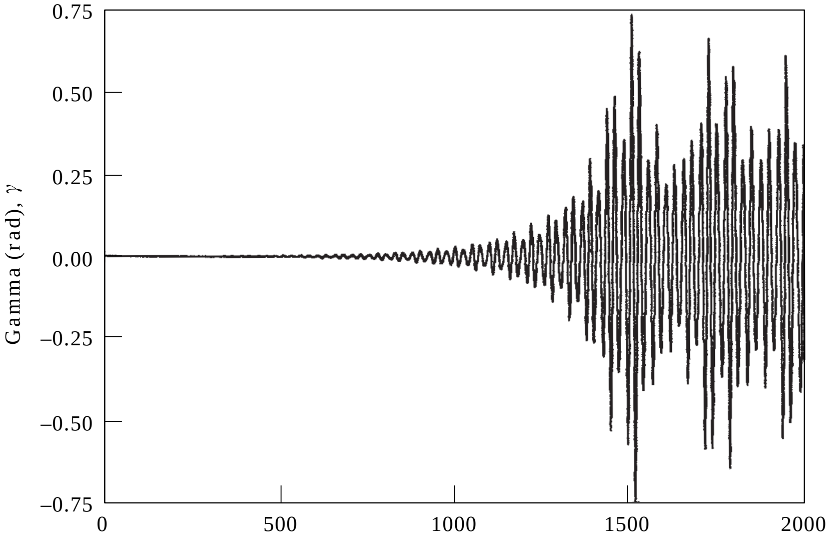

Figure 15. Response to initial conditions: non-linear model.

For stable points the linear and non-linear models were found to be in excellent agreement.

## 8. FORCED MOTIONS

In this section forced instabilities of the systems described by equations (21) (rigid) and (31) (flexible) will be investigated.

Forced motions of ordinary differential equations with time dependent coefficients have been studied extensively. See, for example, the recent work of Kang *et al*. [23]. Here a few observations will be made that are in no way meant to be exhaustive.

Of primary concern is whether new types of instability can occur. For example, Beale [24], using an extension of Hsu's method [25], showed resonances characterized by linear growth were possible when the forcing frequency $\Omega$ is related to the natural frequencies $\Omega_n$ by

$$\Omega = \frac{\Omega_{n_i}}{j}, \qquad i = 1, 2, 3 \ldots, \qquad j = 1, 2, 3 \ldots.$$

For the current models, this condition translates, in dimensionless terms, to

$$\nu = \frac{\nu_{n_i}}{2j}, \qquad i = 1, 2, 3 \ldots, \qquad j = 1, 2, 3 \ldots. \tag{41}$$

No asymptotic solutions exist for the present models. Also the presence of damping makes the applicability of equation (41) to the present system questionable. Nonetheless, resonance points predicted by equation (41) were explored numerically for a few cases. The results were obtained using direct

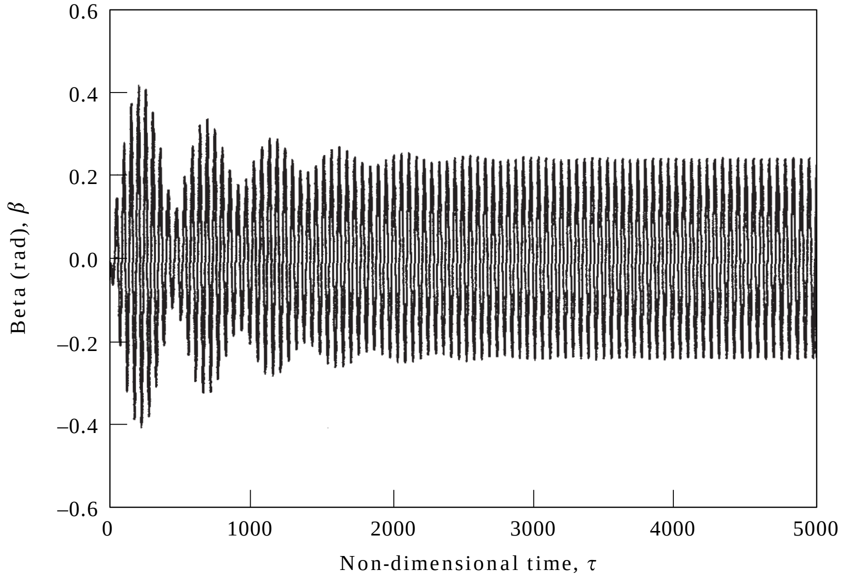

Figure 16. Response of forced system: rigid body linear model ($\Gamma$ = 0·0002, $\nu$ = 0·0605—candidate point for forced resonance).

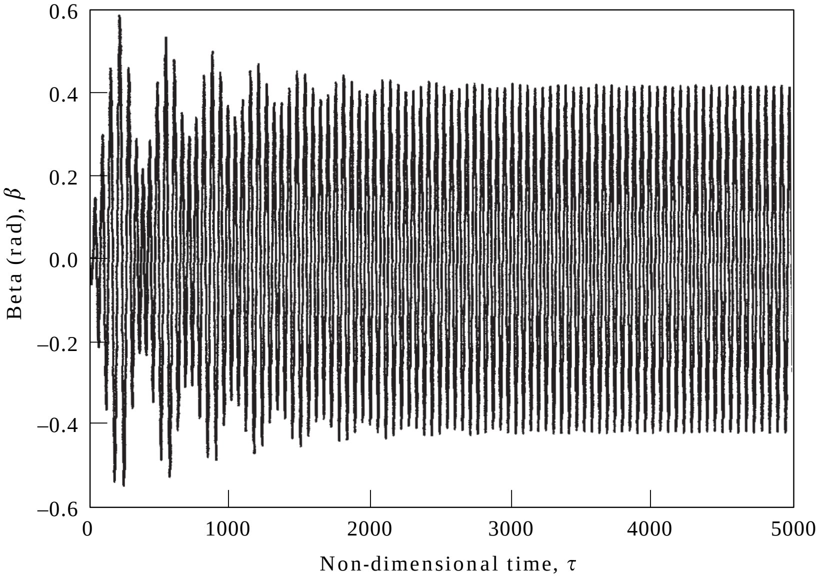

Figure 17. Response of forced system: rigid body non-linear model.

numerical integration of the equations of motion subjected to zero initial conditions.

Only results for the laboratory model are given. From equation (41) a rotational speed that can lead to potential forced instability is $v = 0{\cdot}0605$. Shown in Figures 16 and 17 are the responses for this rotational speed for a torque level of $\Gamma = 0{\cdot}0002$ (which corresponds to a point outside the parametric instability

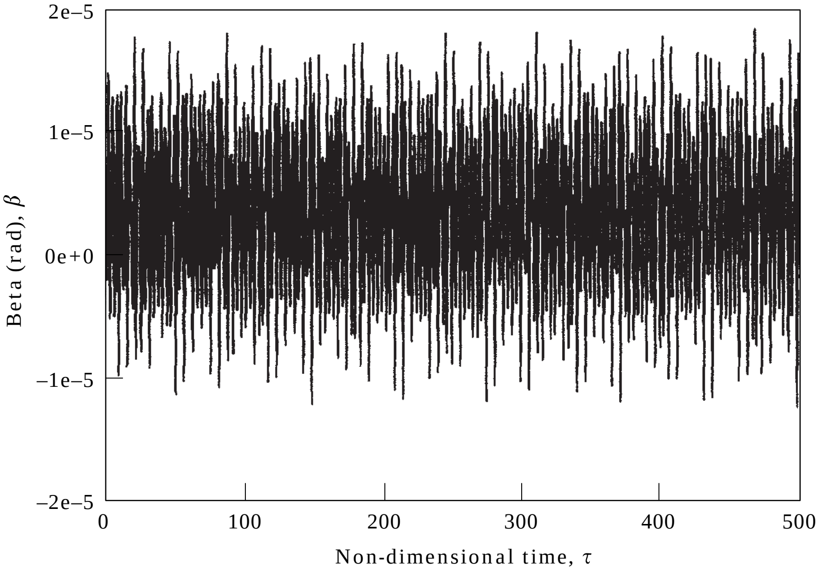

Figure 18. Response of forced system: rigid body linear model ($\Gamma = 0{\cdot}0002$, $v = 0{\cdot}0400$— not a candidate point for forced resonance).

zones). Figures 16 and 17 give the response for the linear and non-linear models, respectively. Several points can be made. There is indeed an initial region of linear growth (zooms confirmed this), but the final motion is bounded. However, the peak amplitudes are quite large (so large in fact, that the linear model breaks down). The steady state amplitude given by the non-linear model is 28°, so for practical purposes the system can be regarded as unstable.

A type of forced resonance has indeed occurred. This point can be further amplified by inspection of Figure 18 which shows the response at the same level of torque but at a rotational speed $v = 0{\cdot}04$, not a candidate for forced resonance. Very small amplitudes are seen (well within the linear range).

Similar results were found for the flexible model. It should be noted that there are more possibilities for forced motion resonance in the flexible model, because of the larger number of natural frequencies involved.

Instabilities were also found at frequencies corresponding to predominantly rigid modes. However, the values for the amplitudes (at steady state) obtained by using the flexible model were found to be larger than the ones obtained via the rigid model. The reason for the difference was attributed to the inclusion of flexibility. For instance, the steady state value at a rotational speed $v = 0{\cdot}0605$ and torque $\Gamma = 0{\cdot}0002$, given by the flexible model, is roughly 0·70 mm at the shaft's midpoint. By using the rigid model the value obtained is about 0·23 mm. The static deflection at that point was calculated, using a one-term Galerkin approximation, and led to a value of 0·53 mm, which shows that the static deflection due to flexibility accounts for the difference.

A potential forced instability was checked for a rotational speed $v = 0{\cdot}7815$ and a value of torque $\Gamma = 0{\cdot}0002$. Note that this speed corresponds to a possible forced resonance frequency for the flexible mode occurring at $v_n = 1{\cdot}5630$ (see equation (41)). Again a linear growth of the response was observed.

## 9. SUMMARY AND CONCLUSIONS

Numerical results were presented for two different sets of physical parameters, a so-called laboratory model and a model utilizing automotive proportions.

For both the linear, rigid and flexible systems, flutter instabilities were found to exist for all values of rotational speed and torque when the damping was zero, for both laboratory and automotive models. However, small values of damping were shown to move the zones outside practical operational ranges. A few point checks using the non-linear rigid body system led to the same conclusions.

In terms of parametric instabilities, it was found that the bending moments can cause strong parametric instabilities in the system (note that the bending moments had to be properly modelled, by the inclusion of the slope of the bent shape at the U-Joint, in the flexible system to capture this effect). The follower torque also led to instabilities which, when compared to the ones caused by the bending moments, were found to be weak. The fluctuating driven shaft rotational speed led to parametric instabilities as well. These were also weak compared to the ones caused by the bending moments.

Several types of parametric instability zones were found to exist in the models. These are zones of principal parametric instability, sum-type combination zones and difference-type combination zones, involving rigid modes (the shaft bouncing on the bearing springs), flexible modes and combination of the predominantly rigid and flexible modes.

The parametric zones involving predominantly rigid modes were found to be of significant size and to occur at practical operating conditions in the laboratory and automotive models. Parametric zones involving flexible modes (and combination with predominantly rigid modes) were also found to occur in a practical range of operational conditions for the laboratory model. For the automotive example, the zones due to flexibility and combination flexible–predominantly rigid modes occurred outside the range of operation. It should be noted that the inclusion of flexibility in the modelling did not affect the parametric zones due to the predominantly rigid modes.

An increase in bearing damping will stabilize the system since the zones of parametric instability occur for higher values of torque as the damping increases. For the laboratory model, an increase in damping more severely affected the difference combination type zones of parametric instability. Sum-type zones and principal zones were also affected but to a lesser degree. A procedure was suggested in order to reduce or eliminate the parametric instabilities. In the automotive case the current models suggest that values of $C_x = C_y = 5{\cdot}0$ N/(m/s) for the damping coefficients would eliminate parametric instabilities from the practical range of operation. Whether such damping levels can be physically attained remains to be explored.

In terms of forced instabilities, forced resonances were found to be possible, in both models, when the rotational speed reached a value corresponding to a natural frequency of the system divided by two. Also, it was found that flexibility was important in terms of the final steady state value for the forced response of the driven shaft. In using the flexible model, the steady state values of the displacements are larger than the ones obtained by using the rigid model.

## REFERENCES

1. H. P. LEE, T. H. TAN and S. B. LENG 1997 *Journal of Sound and Vibration* **199**, 401–415. Dynamic stability of spinning Timoshenko shafts with a time–dependent spin rate.
2. C. W. LEE and J. S. YUN 1996 *Journal of Sound and Vibration* **192**, 439–452. Dynamic analysis of flexible rotors subjected to torque and force.
3. R. L. ESHLEMAN and R. A. EUBANKS 1969 *ASME Journal of Engineering for Industry* **91**, 1180–1188. On the critical speeds of a continuous rotor.
4. H. ZIEGLER 1968 *Principles of Structural Stability*. Waltham, MA: Blaisdell Publishing Company.
5. H. LEIPHOLZ 1987 *Stability Theory—An introduction to the Stability of Dynamic Stystems and Rigid Bodies*. New York: Wiley.
6. N. KHADER 1997 *Journal of Sound and Vibration* **207**, 287–299. Stability analysis for the dynamic design of rotors.

7. R. H. PLAUT and J. WAUER 1995 *Journal of Sound and Vibration* **183**, 889–897. Parametric, external and combination resonances in coupled flexural and torsional oscillations of an unbalanced rotating shaft.
8. C.-W. LEE 1993 *Vibration Analysis of Rotors*. Boston, MA: Kluwer Academic Press.
9. H. OTA and M. KATO 1984 *Bulletin of JSME* **27**, 2002–2007. Lateral vibrations of a rotating shaft driven by a universal joint—1st report.
10. H. OTA, M. KATO and H. SUGITA 1985 *Bulletin of JSME* **28**, 1749–1755. Lateral vibrations of a rotating shaft driven by a universal joint—2nd report.
11. M. KATO and H. OTA 1990 *Journal of Vibration and Acoustics* **112**, 298–303. Lateral excitation of a rotating shaft driven by a universal joint with friction.
12. P.-P. SHEU, W.-H. CHIENG and A.-C. LEE 1996 *Journal of Vibration and Acoustics* **118**, 88–99. Modeling and analysis of the intermediate shaft between two universal joints.
13. M. SAIGO, Y. OKADA and K. ONO 1997 *Journal of Vibration and Acoustics* **119**, 221–229. Self-excited vibration caused by internal friction in universal joints and its stabilizing method.
14. S. F. ASOKANTHAN and M. C. HWANG 1996 *Journal of Vibration and Acoustics* **118**, 368–374. Torsional instabilities in a system incorporating a Hooke's joint.
15. S. F. ASOKANTHAN and X. H. WANG 1996 *Journal of Sound and Vibration* **194**, 83–91. Characterization of torsional instabilities in a Hooke's joint driven system via maximal Lyapunov exponents.
16. R. M. ROSENBERG 1958 *ASME Journal of Applied Mechanics* **25**, 47–51. On the dynamical behavior of rotating shafts driven by universal (Hooke) couplings.
17. T. IWATSUBO and M. SAIGO 1984 *Journal of Sound and Vibration* **95**, 9–18. Transverse vibration of a rotor system driven by a Cardan joint.
18. D. T. GREENWOOD 1988 *Principles of Dynamics*. Englewood Cliffs, NJ: Prentice–Hall.
19. A. J. MAZZEI, JR. 1998 *Doctoral Thesis*, *The University of Michigan*, *Ann Arbor*. Dynamic stability of a flexible spring mounted shaft driven through a universal joint.
20. K. M. HEAL, M. L. HANSEN and K. M. RICHARD 1996 *Maple V—Learning Guide*. New York: Springer–Verlag.
21. L. MEIROVITCH 1970 *Methods of Analytical Dynamics*. New York: McGraw–Hill.
22. M. CARTMELL 1990 *Introduction to Linear*, *Parametric and Nonlinear Vibrations*. New York: Chapman & Hall.
23. Y. KANG, Y.-P. CHANG and S.-C. JEN 1998 *Journal of Sound and Vibration* **209**, 473–492. Strongly non-linear oscillations of winding machines, part I: mode-locking motion and routes to chaos.
24. D. G. BEALE 1988 *Doctoral Thesis*, *The University of Michigan*, *Ann Arbor*. A study of the motion of a flexible rod in a quick return mechanism.
25. C. S. HSU 1963 *Journal of Applied Mechanics* **30**, 367–372. On parametric excitation of a dynamical system having multiple degrees of freedom.
26. M. D. GREENBERG 1978 *Foundations of Applied Mechanics*. Englewood Cliffs, NJ: Prentice–Hall.

## APPENDIX A: GALERKIN COEFFICIENTS

$$\int_0^1 \frac{\mathrm{d}^4\Phi_m}{\mathrm{d}Z^4}(Z)\Phi_i(Z)\,\mathrm{d}Z = \alpha_{1_{mi}}, \qquad \int_0^1 \frac{\mathrm{d}^4\Psi_m}{\mathrm{d}Z^4}(Z)\Psi_i(Z)\,\mathrm{d}Z = \alpha_{2_{mi}},$$

$$\int_0^1 \Phi_m(Z)\Phi_i(Z)\,\mathrm{d}Z = \gamma_{1_{mi}}, \qquad \int_0^1 \Psi_m(Z)\Psi_i(Z)\,\mathrm{d}Z = \gamma_{2_{mi}},$$

$$\int_0^1 \Phi_m(Z)|_{Z=1}\Phi_i(Z)\Lambda(Z-1)\,\mathrm{d}Z = \Phi_m(Z)|_{Z=1}\Phi_i(Z)|_{Z=1} = \xi_{1_{mi}},$$

$$\int_0^1 \Psi_m(Z)|_{Z=1}\Psi_i(Z)\Lambda(Z-1)\,\mathrm{d}Z = \Psi_m(Z)|_{Z=1}\Psi_i(Z)|_{Z=1} = \xi_{2_{mi}},$$

$$\int_0^1 \left.\frac{\mathrm{d}\Psi_m(Z)}{\mathrm{d}Z}\right|_{z=0} \Phi_i(Z)\frac{\mathrm{d}\Lambda(Z)}{\mathrm{d}Z}\,\mathrm{d}Z = -\left.\frac{\mathrm{d}\Psi_m(Z)}{\mathrm{d}Z}\right|_{z=0} \left.\frac{\mathrm{d}\Phi_i(Z)}{\mathrm{d}Z}\right|_{z=0} = -2\delta_{3_{mi}},$$

$$\int_0^1 \left.\frac{\mathrm{d}\Phi_m(Z)}{\mathrm{d}Z}\right|_{z=0} \Psi_i(Z)\frac{\mathrm{d}\Lambda(Z)}{\mathrm{d}Z}\,\mathrm{d}Z = -\left.\frac{\mathrm{d}\Phi_m(Z)}{\mathrm{d}Z}\right|_{z=0} \left.\frac{\mathrm{d}\Psi_i(Z)}{\mathrm{d}Z}\right|_{z=0} = -2\delta_{2_{mi}},$$

$$\int_0^1 \left.\frac{\mathrm{d}\Phi_m(Z)}{\mathrm{d}Z}\right|_{z=0} \Phi_i(Z)\frac{\mathrm{d}\Lambda(Z)}{\mathrm{d}Z}\,\mathrm{d}Z = -\left.\frac{\mathrm{d}\Phi_m(Z)}{\mathrm{d}Z}\right|_{z=0} \left.\frac{\mathrm{d}\Phi_i(Z)}{\mathrm{d}Z}\right|_{z=0} = -2\delta_{1_{mi}},$$

$$\int_0^1 \left.\frac{\mathrm{d}\Psi_m(Z)}{\mathrm{d}Z}\right|_{z=0} \Psi_i(Z)\frac{\mathrm{d}\Lambda(Z)}{\mathrm{d}Z}\,\mathrm{d}Z = -\left.\frac{\mathrm{d}\Psi_m(Z)}{\mathrm{d}Z}\right|_{z=0} \left.\frac{\mathrm{d}\Psi_i(Z)}{\mathrm{d}Z}\right|_{z=0} = -2\delta_{4_{mi}},$$

$$\int_0^1 \frac{\mathrm{d}^3\Psi_m}{\mathrm{d}Z^3}(Z)\Phi_i(Z)\,\mathrm{d}Z = \beta_{1_{mi}}, \qquad \int_0^1 \frac{\mathrm{d}^3\Phi_m}{\mathrm{d}Z^3}(Z)\Psi_i(Z)\,\mathrm{d}Z = \beta_{2_{mi}},$$

$$\int_0^1 \frac{\mathrm{d}^2\Phi_m}{\mathrm{d}Z^2}(Z)\Phi_i(Z)\,\mathrm{d}Z = \lambda_{1_{mi}}, \qquad \int_0^1 \frac{\mathrm{d}^2\Psi_m}{\mathrm{d}Z^2}(Z)\Psi_i(Z)\,\mathrm{d}Z = \lambda_{2_{mi}},$$

$$\int_0^1 \frac{\mathrm{d}^2\Psi_m}{\mathrm{d}Z^2}(Z)\Phi_i(Z)\,\mathrm{d}Z = \lambda_{3_{mi}}, \qquad \int_0^1 \frac{\mathrm{d}^2\Phi_m}{\mathrm{d}Z^2}(Z)\Psi_i(Z)\,\mathrm{d}Z = \lambda_{4_{mi}},$$

$$\int_0^1 \Phi_m(Z)\frac{\mathrm{d}\Lambda(Z)}{\mathrm{d}Z}\,\mathrm{d}Z = -\Phi_m'(0), \qquad \int_0^1 \Psi_m(Z)\frac{\mathrm{d}\Lambda(Z)}{\mathrm{d}Z}\,\mathrm{d}Z = -\Psi_m'(0).$$

The following properties of the Dirac delta function were used [26] in deriving some of the above results:

$$\int_a^b \Delta(Z-\varsigma)g(Z)\,\mathrm{d}Z = g(\varsigma), \qquad \int_a^b \frac{\mathrm{d}\Delta(Z-\varsigma)}{\mathrm{d}Z}g(Z)\,\mathrm{d}Z = -\left.\frac{\mathrm{d}g(Z)}{\mathrm{d}Z}\right|_{Z=\varsigma},$$

$$a < \varsigma < b.$$